Sun glitter Imagery of Ocean Surface Waves. Part 1: Directional spectrum retrieval and validation

by

Vladimir Kudryavtsev[1,2], Maria Yurovskaya[2], Bertrand Chapron[3], Fabrice Collard[4], Craig Donlon[5]

1) *Russian State Hydrometeorological University, St. Petersburg, Russia*

2) *Marine Hydrophysical Institue RAS, Sebastopol, Russia*

3) *Institut Francais de Recherche pour l'Exploitation de la Mer, Plouzané, France*

4) *OcenDataLab, Brest, France*

5) *European Space Agency, Noordwijk, The Netherlands*

Abstract

A practical method is suggested to quantitatively retrieve directional spectra of ocean surface waves from high-resolution satellite sun glitter imagery (SSGI). The method builds on direct determination of the imaging transfer function from the large-scale smoothed shape of sun glitter. Observed brightness modulations are then converted into sea surface elevations to perform directional spectral analysis. The method is applied to the Copernicus Sentinel-2 Multi-Spectral Instrument (MSI) measurements. Owing to the specific instrumental configuration of MSI (which has a primary mission dedicated to mapping land surfaces), a physical angular difference between channel detectors on the instrument focal plane array can be used to efficiently determine the surface brightness gradients in two directions, i.e. in sensor zenith and azimuthal directions. In addition, the detector configuration of MSI means that a small temporal lag between channel acquisitions exists. This feature can be exploited to detect surface waves and infer their space-time characteristics using cross-channel correlation. We demonstrate how this can be used to remove directional ambiguity in 2D detected wave spectra, and to obtain information describing local dispersion of surface waves. Directional spectra derived from Sentinel-2 MSI SSGI are compared with in situ buoy measurements. We report an encouraging agreement between SSGI-derived wave spectra and in situ measurements.

1. Introduction

Space-borne instruments operating in the visible range of the electromagnetic spectrum can precisely capture fine contrast modulations related to local changes of the specular reflections of visible sunlight on the highly sensitive ocean facets. Very often ocean satellite sun glitter views strongly resemble ocean synthetic aperture radar (SAR) images, in that the fine scale structures and patterns at ocean surface can be precisely delineated, with meandering surface slicks and fronts, internal waves and surface gravity waves clearly expressed.

As originally demonstrated by Cox and Munk (1954) with airborne measurements, and confirmed from space-borne measurements (e.g. Bréon and Henriot, 2006), Satellite Sun Glitter Imagery (SSGI) contains valuable information on directional statistical properties of the wind-ruffled sea surface roughness (Barber, 1954), especially its mean square slope (MSS), skewness and kurtosis. Local modulations of the detected SSGI brightness measurements by upper ocean dynamic processes affect SSGI statistical properties, especially sea surface roughness MSS, revealing spectacular patterns. For instance, using SSGI, Apel et al. (1975) observed and studied non-linear internal wave properties. Later, Jackson (2007), using MODIS SSGI observations, derived a global distribution of internal waves. SSGI of surface slicks have also been often reported, e.g. Hu et al. (2009), and a practical approach to convert sun glitter brightness variations into MSS anomalies was suggested by Kudryavtsev et al. (2012a, 2012b) to quantify satellite observations of oil spills and sub-mesoscale ocean currents (e.g. Rascle et al., 2014).

At very high spatial resolution, ocean waves can be resolved and imaged in SSGI, with the potential to reveal wave transformations and impressive refraction patterns (e.g., Figure 8a in Genz et al., 2009). Under favourable conditions, the sunlight reflected by the ocean wave slopes produces glints in the SSGI according to the relative positions between the sensor, the wave front geometry, the sun azimuth and its elevation. Local surface slopes associated with long surface waves (swell and spectral peak of wind-generated waves) have corresponding variations of the SSGI brightness. Besides the obvious requirement for cloud-free conditions, this technique depends upon the instrumental configuration for which the sun, the instrument, and the ocean wave field are in a favourable alignment. For these reasons, optical techniques have a limited development compared to radar, especially SAR, methods (e.g., Collard et al., 2005). Nevertheless, a large number of studies have demonstrated the potential operational use of airborne optical imaging systems to study ocean swell spectra especially for coastal applications (e.g., Stillwell, 1969, Dugan et al., 2001, Gelpi et al., 2001).

Using airborne photography, it is straightforward to covert wave induced modulations of the SSGI brightness into 2D spectra of the surface elevations using a modulation transfer function. Bolshakov et al. (1988) defined this transfer function by extending the Cox and Munk (1954) model to account for the image-resolved surface waves. The authors did not prescribe any model for the probability density function (PDF) of the small-scale (unresolved) wave slopes but used directly the shape of the SSGI as proxy of the real PDF. Very good agreement between 2D wave elevation spectra derived from SSGI and in situ measurements were reported (Bolshakov et al. 1990a, 1990b), including comparisons with empirical fetch-law development for young wind seas. Gelpi et al. (2001) also defined the transfer function by extending the Cox and Munk (1954) model, but considered an idealized Gaussian PDF and a good agreement between the optically derived wave spectra and buoy measurements was also found.

Contrary to airborne photography, satellite optical instruments usually provide surface brightness measurements in only one particular direction. For instance, measurements from the ENVISAT Medium Resolution Imaging Spectrometer (MERIS), are made in a “push-broom" mode: linear CCD arrays provide spatial sampling in the across-track direction (vertically beneath the instrument at nadir) and successive samples are acquired in the along-track direction that the ENVISAT satellite flies. Such a configuration may not be always optimal to investigate ocean processes because the SSGI provide measurements in only one cross-track direction, and the proper 2D information of the brightness field is not available (see Kudryavtsev et al., 2012a for more detailed discussion).

Owing to its specific instrumentation and configuration, the Copernicus Sentinel-2 (S2) Multi-Spectral Instrument (MSI) optical instrument (e.g., ESA, 2012) is not subject to such a limitation and can determine the SSGI surface brightness gradients in both the sensor zenith and sensor azimuth directions, see Fig.1. Furthermore, the related short-time lag between the cross-channel measurements (e.g. time lag between "red" bands B8 and B8A is about 2 sec) provides an additional opportunity to study the space-time characteristics of the detected surface wave field (see e.g. Michele et al., 2012). S2 MSI cross-channel parallax provides an optimal time lag which is long enough to estimate phase velocity of ocean waves and, at the same time, short enough to maintain a strong coherence between the two consecutive observations. Together with a sufficiently high ground resolution of 10m for channels B04 (665 nm) and B08 (842 nm), the S2 MSI measurements is an interesting instrument to implement and test SSGI retrieval methods previously developed for airborne sun glitter photography.

(Figure 1 is about here)

In this paper, we first recall the method to retrieve directional spectra of ocean surface waves from high resolution SSGI. In section 3 the technique is then applied to S2 MSI data acquired over in situ directional buoy measurements and a verification analysis is presented. Our conclusions and suggestions are then given Section 4.

2. 2D wave spectra retrieval from SSGI

Over the ocean, satellite optical images collected during daylight contain distinct silvery-grey ellipses of sea surface reflected sunlight within approximately 30 degree of the Sun's specular reflection point. To more efficiently probe surface roughness variations, "red" spectral channels (~800-900 nm) are the most useful because light is only absorbed within a very "thin" surface layer and, thus, derived SSGI is not too sensitive to the optical properties of the upper water column.

2.1. SSGI brightness variations

We consider the surface brightness field in the sun glitter area where the impact of the sky radiance reflected from the surface is negligible. Following Cox and Munk (1954), the sun glitter radiance, B, generated by specular reflection of the sun light is given by

$$B = \frac{\rho E_s}{4 \cos\theta_v \cos^4 \beta} P(Z_1, Z_2, S) \tag{1}$$

where E_s is the solar irradiance, ρ is the Fresnel reflection coefficient, θ_v is the view zenith angle, P is the 2D probability density function (PDF) of the sea surface slopes z_1 and z_2 in two orthogonal directions x_1 and x_2 correspondingly, S is a generalized sea surface slope parameter. This parameter states that P is dependent on statistical properties of the sea surface slopes, like mean square slope (MSS), skewness and peakedness; capital Z_1 and Z_2 in (1) denote the sea surface slopes satisfy the conditions of specular reflections

$$Z_1 = -\frac{\sin\theta_s \cos\varphi_s + \sin\theta_v \cos\varphi_v}{\cos\theta_s + \cos\theta_v}$$
$$Z_2 = -\frac{\sin\theta_s \sin\varphi_s + \sin\theta_v \sin\varphi_v}{\cos\theta_s + \cos\theta_v} \qquad (2)$$

where θ_s and θ_v are the sun and the sensor zenith angles correspondingly, φ_v and φ_s are the view and sun azimuth angles, and $\tan\beta = \sqrt{Z_1^2 + Z_2^2}$.

Cox and Munk (1954) and, later, e.g. Chapron et al. (2000) and Bréon and Henriot (2006), modelled the 2D sea surface PDF as non-Gaussian, taking into account the non-linearity of the surface wave slopes. Hereafter, we do not use any PDF model. Instead, we directly rely on the observed 2D large-scale shape of the sun glitter as a proxy of the local sea surface slopes PDF.

Let us represent the PDF, P, in (1) in a normalized form:

$$P(Z_1, Z_2) = s^{-2} p(Z_1/s, Z_2/s) \qquad (3)$$

where s^2 is the mean squared slope (MSS) of the sea surface, and p is a “scaled” PDF. In (3), following Kudryavtsev et al. (2012a), we assume that s^2 dominates and controls variations of other statistical parameters of the surface slopes, in particular the slope directionality, peakedness and skewness. In other words, it is assumed that the magnitude of the relative MSS variations $\tilde{s}^2 / s_0^2$ is significantly larger than variations of other sea slope statistical moments $\overline{z_1^m z_2^n}$ scaled by the MSS, $c_{mn} = \overline{z_1^m z_2^n} / s^{m+n}$, i.e. $\tilde{s}^2 / s^2 \gg \tilde{c}_{mn} / c_{mn}$. This assumption is largely supported by the measurements from Cox and Munk (1954), and Kudryavtsev et al. (2012a) provides a more in-depth discussion. Equation (1) is then rewritten in the form

$$B' \equiv B\cos\theta_v = \frac{1}{4}\rho E_s (1+Z_n^2)^2 s^{-2} p\left(Z_j/s\right) \quad (4)$$

where $Z_n = \sqrt{Z_j Z_j}$, subscript j varies from 1 to 2 (for the remainder of this paper repeated indexes presumes summing up). Following from (4), B' is a function of two variables Z_j and s^2. The MSS is mostly supported by wind waves shorter than O(1) m (Vandemark et al., 2004) and accordingly, the overall shape of the sun glitter is dependent on statistical properties of these short wind waves (i.e. wavelengths in the range from millimetres to meters). Long surface waves, swell and/or wind waves near their spectral wind peak will tilt and modulate the shorter waves.

Tilt and hydrodynamic modulations result in directional brightness variations on the scale of modulating long waves (image-resolved waves), LW, as

$$B' = \frac{1}{4}\rho E_s \frac{\left[1+(Z_1+\varsigma_1)^2+(Z_2+\varsigma_2)^2\right]^2}{(s_0+\tilde{s})^2} p\left(\frac{Z_j+\varsigma_j}{s_0+\tilde{s}}\right) \quad (5)$$

where ς_j is local slopes of LW in x_j direction, s_0 and $\tilde{s}$ are mean and variations of the surface slopes standard deviations (STD) caused by LW. After decomposition of the brightness field $B' = B_0' + \tilde{B}'$ into a background part B_0' and LW-induced variations $\tilde{B}'$, the linearized equation (5) reads:

$$\tilde{b} \equiv \tilde{B}'/B_0' = G_{zj}\varsigma_j - T\,\widetilde{s^2}/s_0^2 \quad (6)$$

where $G_{zj} = (1/B_0^{'})\partial B_0^{'}/\partial Z_j$ is the component of the sunglitter brightness gradient over the specular slopes, and T is a transfer function describing response of the surface brightness to the MSS variations:

$$T = \frac{1}{2} G_{zj} Z_j + \frac{1 - Z_j Z_j}{1 + Z_j Z_j} \quad (7)$$

If we average (6) over LW scales, the first term in the right hand side vanishes, to arrive at an equation relating the sunglitter brightness variation to MSS anomalies, caused by short wave damping in slicks, and/or by interactions with surface currents, e.g. internal waves and fronts (Kudryavtsev et al., 2012a, 2012b; Rascle et al., 2014).

2.2. Role of hydrodynamic modulations

In the present context, the modulation of the MSS by LWs is a factor that could hinder direct reconstruction of the LW slopes from sun-glitter brightness modulations. Note, the transfer function T is vanishing in the vicinity of a so-called zone of contrast inversion. In a sun glitter image, this zone approximately corresponds to the area where $Z_n^2 \approx s^2$. Using airborne photographs, this zone of contrast inversion can easily be identified, e.g. windrow type stripes change their contrast from darkish (in the “outer” part of the sunglitter) to bright (in the “inner” sunglitter part). When performing spectral processing analysis, Bolshakov et al. (1988, 1990a) suggested that these particular image areas are selected to minimize the impact of MSS modulations on the derived 2D wave spectra elevation. Thorough analysis of the impact of the contrast inversion zone (a critical sensor viewing angle) on satellite sun-glitter imaging of the oceanic and atmospheric phenomena can be found in (Jackson and Alpers, 2010).

Satellite sun glitter images (SSGI) do not always provide proper locations of these contrast inversion areas. Therefore we must evaluate the expected contribution of the MSS modulations on the accuracy of the LW spectra retrieval. Although considered method is free of the PDF model specification, we need to specify it here in order to get quantitative estimates of the expected contribution. As a first guess, we assume the sea surface PDF is Gaussian and azimuthally isotropic, and specify it as:

$$p = \frac{1}{\pi}\exp\left(-Z_n^2 \big/ s^2\right) \tag{8}$$

In this case, components G_{zj} of the brightness gradient are

$$\begin{aligned} G_{zj} &= -\frac{2Z_j}{s^2}\left(1 - \frac{2s^2}{1+Z_n^2}\right) \\ &\approx -2\,Z_j \big/ s^2 \end{aligned} \tag{9}$$

where the approximation follows from $s^2 \ll 1$. Brightness variation (6) reads

$$\tilde{b} = -2s^{-2} Z_j \varsigma_j - \left(1 - Z_n^2 \big/ s^2\right)\widetilde{s^2} \big/ s^2 \tag{10}$$

If the LW are monochromatic with amplitude A and wavenumber K, then $Z_j\varsigma_j = iAKZ_n\cos\phi$, and $\widetilde{s^2}\big/s^2 = M_s AK$, where ϕ is the angle between wavenumber vector and direction of the mean brightness gradient, and M_s is the complex modulation transfer function, MTF, for the MSS. If the second term on the right-hand side of (10) is omitted, it corresponds to the algorithm suggested by Gelpi et al. (2001, their Eq. (11) and (12)) to retrieve of the surface wave spectrum, using the Cox and Munk (1954) model with a Gaussian PDF approximation.

Following from (10), the ratio of the MSS and tilt modulation contributions to the squared amplitude of brightness modulations is

$$r = \left[\frac{sM_s \left(1 - Z_n^2 / s^2\right)}{2\cos\phi Z_n / s} \right]^2 \tag{11}$$

To evaluate (11), M_s is defined as

$$M_s = \iint M(\boldsymbol{k}) \mathrm{B}(\boldsymbol{k}) d\varphi d\ln k \Big/ \iint \mathrm{B}(\boldsymbol{k}) d\varphi d\ln k \tag{12}$$

where $\mathrm{B}(\boldsymbol{k})$ is the saturation spectrum, and M is the spectral MTF. As mentioned above, wind waves containing most of the MSS are rather short and thus their corresponding group velocity is much smaller than the LW phase velocity. To obtain the upper estimate of M_s, we assume the short waves to travel along LW as free waves. In this case, the modulation of short waves by LW is described by the conservation of wave action, N, (Phillips, 1977)

$$\frac{\partial \tilde{N}}{\partial t} - k_j \frac{\partial u_j}{\partial x_i} \frac{\partial N_0}{\partial k_i} = 0 \tag{13}$$

Solution of (13) in terms of the short wave MTF, $M = \hat{N} / (N_0 AK)$ (hat denotes amplitude of modulations), reads

$$M = m_k \cos^2 \varphi \tag{14}$$

where m_k is the wavenumber exponent of the wave action spectrum. In the right-hand side, we only retain the term which provides a non-zero contribution to integral properties of short waves, like MSS modulations defined by (12), (see Kudryavtsev et al. 2005, their eq.(44) and (46) and discussion therein). For B, which is almost constant (i.e., the Phillips spectrum), then m_k = - 9/2, and M_s defined by (12) with (14) can be taken as M_s = 9/4.

The ratio between hydrodynamic and tilt modulations (11) is shown in Fig.1. Around the center of the sun glitter, $Z_n^2/s^2 \approx 0$, as well as in the vicinity of the direction perpendicular to the brightness gradient, $\cos\phi = 0$, tilt modulations vanish, and thus, LW can solely be visible due to MSS hydrodynamic modulations. In the vicinity of the contrast inversion, $Z_n^2/s^2 \approx 1$, MSS modulations vanish. This sun glitter area is thus the preferable location to derive LW parameters, as brightness modulations are solely linked to the LW slopes.

(Figure 2 is about here)

As shown in Fig. 2, calculations for different wind speeds, and LW directions relative to the brightness gradient, suggest that we can neglect the impact of the MSS modulations within a sun glitter area satisfying 0.3< Z_n^2/s^2 <2. For these configurations, if we do not consider MSS modulations we may expect an error of up to 10% (and less) in the retrieval of LW elevations from SSGI brightness modulations. Hereinafter, we will tolerate such inaccuracy and ignore MSS modulations. Width of the ground track area satisfying condition 0.3< Z_n^2/s^2 <2 is of order $0.7sH$, where H = 876 km is the altitude of S2 satellite. If e.g. $s = 0.2$ (that corresponds to wind speed 7-8 m/s) and sensor azimuth is toward the sun, than the width of the area, where our assumption is valid, is $2 \times 0.7sH$ = 240 km, which is comparable with the width of S2 MSI image, 290 km. Apparently, this is the upper estimate; the real portion of the S2 image applicable for suggested method, depends entirely on sun and viewing geometry. Notice that beyond Z_n^2/s^2 =2, SSGI brightness falls by an order of magnitude relative to its peak value near the center. Therefore, the application of our proposed method at larger Z_n^2/s^2, at Z_n^2/s^2 >2, is strongly questionable due to the increasing contribution of sky radiance.

2.3. Wave spectra retrieval from 2D SSGI

As sea surface slope PDF's can significantly depart from a Gaussian model, it is tempting to determine the gradient of the brightness, G_{zj} in (6), directly from the observations, without an a priori PDF model.

These "natural" characteristics of SSGI are the measured components of the brightness gradient in two perpendicular directions: $G_j = \left(1/B'\right)\partial B'/\partial x_j$. The gradients G_{zj} in (6) can thus be obtained from the "observed" gradients G_j, as:

$$\begin{aligned} G_{z1} &= \left(G_2 Z_{2,1} - G_1 Z_{2,2}\right)/\Delta \\ G_{z2} &= \left(G_1 Z_{1,2} - G_2 Z_{1,1}\right)/\Delta \end{aligned} \tag{15}$$

where $Z_{i,j} = \partial Z_i / \partial x_j$, and Δ, the determinant, defined by $\Delta = Z_{1,2} Z_{2,1} - Z_{1,1} Z_{2,2}$. This approach is self-consistent. The mean (averaged over the dominant wave scales) 2D shape of the sun glitter brightness, $B'(x,y)$, helps define the gradient G_{zj} using (15) which are then used to convert the brightness variation $\tilde{B}' = B' - B'_0$ into the dominant wave slopes following (6). With MSS modulations omitted, (6) in Fourier space reads

$$\hat{b}(\boldsymbol{K}) = G_{zj} K_j \hat{\varsigma}(\boldsymbol{K}) \tag{16}$$

where the hat over a variable denotes its Fourier transform, and $\hat{b} = \hat{B}'/B'_0$. This equation can further be used to reconstruct the sea surface elevation field via inverse Fourier transformation:

$$\varsigma(\boldsymbol{x}) = \int \hat{b}(\boldsymbol{K}) / \left(G_{zj} K_j\right) \exp\left(K_j x_j\right) d\boldsymbol{K} \tag{17}$$

This relation contains a singularity around $G_{zj}K_j = 0$ which can be removed (as a first guess) assuming that the narrow sector of $\hat{b}(\boldsymbol{K})$ surrounding the line $G_{zj}K_j = 0$, does not contribute to the elevation field.

The spectrum of dominant waves, $S_\varsigma(\boldsymbol{K})$, follows and is derived from the spectrum of sun glitter brightness variations, $S_b(\boldsymbol{K})$, as

$$S_\varsigma(\boldsymbol{K}) = S_b(\boldsymbol{K}) \Big/ \left(G_{zj}K_j\right)^2 \tag{18}$$

Again, there is a singularity in the vicinity $G_{zj}K_j = 0$ where the retrieval of the wave spectrum is impossible. If the SSGI can be obtained over a wide field of view, tiles corresponding to different directions of the brightness gradient can be selected, to help remove the impact of singularity (Bolshakov et al. ,1988, 1990a):

$$S_\varsigma(\boldsymbol{K}) = \sum_n S_b^n(\boldsymbol{K}) \Big/ \sum_n \left(G_{zj}^n K_j\right)^2 \tag{19}$$

where summation is performed over the image tiles selected along different directions of the brightness gradient.

3. Application to Sentinel-2 SSGI

3.1. The data

The Sentinel-2 Multi Spectral Instrument is composed of 12 staggered detectors, which cover the extremely wide 290 km instrument field of view at a maximum ground spatial resolution of 10 m. Due to the staggered positioning of the detectors on the focal planes, a parallax angle between the two alternating odd and even clusters of detectors is induced in the measurements, resulting in a shift along track of approximately 46 km (maximum) inter-detector. Likewise, the hardware design of both the Visible and Near

Infrared (VNIR) and Short Wave Infrared (SWIR) detectors imposes a relative displacement of each spectral channel sensor within the detector resulting in an inter-band measurement parallax amounting to a maximum along track displacement of approximately 14 km. Thus, the odd numbered detectors in the array are looking forward, and the even numbered detectors are looking backward relative to the flight direction of the satellite. Therefore, there is an azimuth difference between successive detector arrays: MSI images exhibit detector wide "stripes" as brightness of observed surface varies with azimuth, Fig.1. For the present study we use "red" channels B04 (wavelength 665 nm) and B08 (wavelength 842 nm). An example of an MSI "striped" SSGI of the ocean surface is shown in Fig. 3.

MSI sensor incidence and azimuth angles are shown Fig. 4, and reveal how brightness stripes originate from the step-like change of the sensor azimuth. This unique feature of the MSI instrument design provides valuable information about the 2D brightness gradient (in incidence and azimuth directions) to retrieve surface wave spectra from SSGI.

(Figure 3 is about here)

(Figure 4 is about here)

The distribution of the surface brightness inside the white rectangle indicated in Fig.3 is shown in Fig. 5. The brightness exhibits a pronounced trend in zenith directions showing a gradual increase of B' with increasing zenith angle for an individual detector strip (along x_1-axis, pixel number linked to the zenith angle), and in azimuth. There is an "abrupt" change of B' at a given x_1 where the azimuth angle switches from one detector strip to the next strip.

(Figure 5 is about here)

Small-scale brightness modulations originating from surface waves are clearly visible. For the given sun and instrument angles, surface slopes, Z_n, providing specular reflections, vary from 0.15 to 0.18. The wind speed over the observation area taken from the buoy (white star in Fig.2) was reported 3.5 m/s. Following Cox and Munk (1954), it suggests s = 0.14. The parameter Z_n/s for this scene is thus close to 1, and therefore provides optimal conditions for surface wave spectra retrieval.

3.2. Wave spectrum retrieval from SSGI

The mean brightness field shown in Fig. 5(b) are used to calculate the mean 2D brightness gradient $G_1 = (1/\bar{B}')\overline{\partial B'/\partial x_1}$ and $G_2 = (1/\bar{B}')\overline{\partial B'/\partial x_2}$, with the x_1-axis directed perpendicular to the satellite flight track (perpendicular to the stripe), and x_2-axis directed along the satellite flight track. The brightness fields of Fig. 5, averaged over x_2 direction inside each of the detector strips, are shown Figure 6a. We define components of the mean brightness gradients as (following notations in Fig. 6a)

$$\begin{aligned} G_1 &= 2(B_4 - B_2)/(B_4 + B_2) \\ G_2 &= (B_1 - B_2)/(B_1 + B_2) + (B_3 - B_4)/(B_3 + B_4) \end{aligned} \tag{20}$$

The similar definition is introduced for the gradients of the specular slopes $Z_{i,j} = \overline{\partial Z_i/\partial x_j}$. Then determination of the tilt transfer function components G_{zj} following (15) is straightforward and an example of calculated G_{zj} is shown in Fig. 6b.

(Figure 6 is about here)

A fragment of the image used for spectral analysis is presented in Fig. 7a and a zoomed image is shown in Fig. 7b that clearly indicates at least two wave systems.

Hereinafter we account the wave directions from the east counter-clockwise. The SSGI brightness contrast spectrum, Fig.7c, clearly exhibits a spectral peak corresponding to waves travelling from 160 deg. and from -20 deg., clearly visible in Fig. 7a. In addition, the brightness spectrum detects weaker spectral features at azimuth 100 deg. and -80 deg, and azimuth 30 deg and -150 deg. Careful inspection of the image zoom, Fig. 7b, indeed visibly confirms the existence of a possible three wave systems (notice that unlike the image fragments, the spectra are rotated, so that k_x-axis is directed to the east).

(Figure 7 is about here)

The wave elevation spectrum shown in in Fig. 7d is calculated from (18) using the brightness spectrum in Fig. 7c and the tilt transfer function of Fig. 6b as input parameters. As discussed, there is a singularity in the vicinity of $G_{zj}k_j = 0$ and this singularity line is approximately consistent with sectors of minimal values in the brightness spectrum.

Application of the transfer function redistributes the spectral energy density in k-space, and clearly enhances the spectral peak of the waves traveling from direction 90 deg and -90 deg.

In the next section, we compare reconstructed spectrum with in situ buoy-measurements, but first we discuss how to remove directional ambiguity using cross-channel analysis.

3.3. Cross-channel analysis

The two S2 MSI channels, B04 (664 nm) and B08 (864 nm), considered in this study, measure the brightness of the same point on the surface with a small time lag. This temporal lag results from angular difference between acquisitions by each channel, as revealed by comparing sensor azimuths for channels B04 and B08 shown in Fig. 4 (specifically, see cross-channel azimuths difference in Fig.4e).

In the first instance, cross-channel time delay can be used to remove the wave propagation directional ambiguity, as demonstrated Fig. 8a and Fig. 8b. The images are highly correlated as confirmed by a high level of coherence in the spectral domain corresponding to the large brightness variations. As expected, the phase spectrum has 180-degree asymmetry. This asymmetry, - sign of the phase spectrum, is further used to remove directional ambiguity of 2D spectra which was already noticed in Fig.7c and Fig.7d. Following the viewing geometry of S2 observation, we introduced a definition stating that negative (resp. positive) phases of cross-spectrum between B04 and B08 channels pick out “true” direction of wave components for descending (resp. ascending) satellite acquisitions.

(Figure 8 is about here)

Following from the linear wave theory, the anticipated phase shift is

$$\begin{aligned}\Phi(k) &= -\omega\Delta t \\ &= -(gk)^{1/2}\Delta t\end{aligned} \tag{21}$$

where Δt is time delay between cross-channel detectors which can be calculated from “instrument azimuths” for each of the MSI channels (see Fig.4 right column, and Fig.4e) as

$$\begin{aligned}\Delta t &= D/V \\ D &= \Delta\varphi_v H \tan\theta_v\end{aligned} \tag{22}$$

where D is ground distance, $H =$ is altitude of the satellite, V is its ground speed, estimated as $V = V_0 R_E/(R_E + H)$, where R_E is the Earth radius, V_0 is the satellite velocity (H and V_0, are taken from Sentinel-2 metadata files), θ_v is mean (between two channels) zenith view angle, and $\Delta\varphi_v$ is azimuth difference. The measured phase minus anticipated (model) phase, calculated using (21) and (22), is shown in Fig. 8c. For this case, Δt is about 0.8 s. The phase of waves travelling in the "true" direction obeys the model predictions. A transect of the cross channel phase, $\Phi(k,\varphi)$, represented in terms of phase velocity

$$\begin{aligned} C &= \Phi(k,\varphi)/(k\Delta t) \\ &= V\,\Phi(k,\varphi)/\left(kH\Delta\varphi_v \tan\theta_v\right) \end{aligned} \tag{22a}$$

at φ=170 deg. (shown in Fig. 8d) is also in very good agreement with the linear-model prediction.

3.4. Comparison with buoy measurements

To help validate the approach we have described, we specifically chose an MSI image that includes an in situ directional wave buoy shown in Fig. 3. The directional buoy and SSGI-computed spectra are shown in Figure 9. The SSGI spectrum is a "true" directional spectrum obtained from the folded spectrum, Fig. 7, and the application of a phase mask (negative/positive values are assigned 1/0), and then multiplying by a factor two to conserve the total energy. As compared to the buoy spectrum, the SSGI spectrum clearly displays a much higher directional resolution. The two spectral peaks, visually corresponding to wave systems in Fig. 7b, are merged in the buoy spectrum, to exhibit a very smeared directional distribution.

Nevertheless, the derived omni-directional SSGI spectrum is found consistent with that computed from the in situ buoy measurements, with a similar spectral level and shape. The significant wave height (SWH, Hs) evaluated from the SSGI spectrum, Hs=1.4 m, is very close to that measured by the buoy, Hs = 1.5 m.

(Figure 9 is about here)

Near the same location as the buoy, a S2 sun glitter image was acquired on 2016-04-19 18:44 and shown in Fig. 10. SSGI data processing was performed in an identical manner to that previously described. The resulting brightness modulation spectrum is reported Fig. 11a. Application of the tilt transfer function enhances a secondary brightness spectrum peak, and the wave elevation spectrum becomes bimodal as shown in Fig. 11b. The bi-modal structure of the surface wave field is confirmed from the image zoom, shown in Fig. 10.

(Figure 10 is about here)

(Figure 11 is about here)

Again, in the spectral domain corresponding to large brightness variations, the cross-channel, B04 and B08, images are highly correlated as shown in Fig. 11c. In addition, phase difference, the difference between observed cross-channel phase and expected model phase (21) shown in Fig. 11d, removes directional ambiguity, and clearly indicates the direction of detected waves.

Comparison of directional and omnidirectional buoy and SSGI spectra is presented in Fig. 12. The SSGI spectrum clearly exhibits a very high angular resolution. It resolves two wave systems very well, apparently merged and smeared in the buoy angular distribution. Omnidirectional spectra, Fig. 12c, are again consistent in terms of both the spectral level and shape, and possess almost the same SWH, Hs=1.3 m and Hs=1.2 m, respectively.

(Figure 12 is about here)

A final case is documented in Fig.13 to Fig.15. Unlike the previous cases, the wave field has a “broad” angular distribution, also revealed visually, Fig. 13, and confirmed from the brightness and the wave elevation spectra, Fig.14. Cross-channel images are still highly correlated (Fig. 14c) and phase shift (Fig. 14d) removes directional ambiguity.

(Figure 13 is about here)

(Figure 14 is about here)

Comparison of directional and omnidirectional spectra is shown in Fig.15. In this case, the SSGI spectrum broad angular distribution is fully consistent with the buoy spectrum. As in the previous cases, SSGI omnidirectional spectrum also agrees with the buoy spectrum, and even reproduces a high-frequency secondary spectral peak around k=0.15 rad/m. SWH following from the sunglitter spectrum is Hs=0.7 m that is consistent with Hs=0.6 m as measured by the buoy.

(Figure 15 is about here)

4. Conclusion

A practical method is proposed and tested to retrieve directional spectra of the surface waves using satellite sun glitter imagery (SSGI) obtained from the Copernicus Sentinel-2 Multi Spectral Instrument (MSI). The short waves, from capillaries to order 1 m gravity waves, contain most of the total mean square slope (MSS) of the sea surface, and are generally not resolved using a satellite sensor. Long waves, near the wind peak wavelength and/or swell, are possibly resolved and mostly contribute to the total wave energy. The SSGI of these long surface waves (LW) can thus be described within the frame of a two-scale model: LW carrying shorter waves (i) provide local tilts, and (ii) modulate short waves leading to MSS variations correlated with LW. Both factors are imaging mechanisms resulting in LW-induced variations of the SSGI brightness.

As proposed, the brightness modulations are converted into LW elevations using a transfer function determined from the smoothed 2D shape of the SSGI. As compared to the contribution of tilt modulations, MSS modulations can be ignored for observations within a SSGI satisfying conditions $0.3 < Z_n^2 / s^2 < 2$.

We demonstrate the proposed methodology using Copernicus Sentinel-2 MSI measurements. Indeed, because of the specific instrumentation and configuration of the MSI multi-channel detectors, MSI data enable us to determine (i) the surface brightness gradients in two directions, - in sensor zenith and sensor azimuth directions, and (ii) space-time characteristics of the surface waves using time delay in cross-channel measurements. This latter property can then be used to remove directional ambiguity in 2D spectra and to evaluate the dispersion of the surface waves. So far, these combined capabilities have been little exploited for ocean applications, especially to quantitatively retrieve ocean swell information.

Compared to in situ measurements, directional spectra derived from Sentinel-2 MSI SSGI are found to be in good agreement. SSGI spectra generally exhibit high angular resolution to help retrieve directional properties of resolved waves. The high coherency at short time lag further helps to robustly retrieve the propagation properties. Finally, shapes of the measured omnidirectional spectra, and SWH estimates, also compare very well to in situ measurements.

While certainly limited to cloud-free areas, and to favourable periods for which the sun, the sensor, and the ocean wave field provide proper geometrical configurations, suggested technic has two main advantages as compared with SAR. First, the cross-channel time lag is about 10 times larger than that can be obtained by extracting multi-looks in any SAR sensor. This is constrained by a limited dwell time, except for SAR spot mode only available on some commercial SAR satellites, and never used over the ocean. This larger time lag translates proportionally in better accuracy of the retrieved wave motion. Second, for Sentinal-2 the imaging principle are the same in two orthogonal directions, along and across track. For SAR, they are different; in the azimuth direction the imaging uses a Doppler based focussing introducing an azimuth cutoff caused by random unresolved ocean wave motions and an overall distortion by orbital velocities of resolved long waves. For this reason, unlike Sentinel-2, SAR is capable to provide quantitative information for long waves only. As compare with altimeter, the clear advantage of suggested technic is the ability to derive 2D spectra describing distribution of the wave energy over the wavelengths and the directions.

These first reported results certainly suggest that Copernicus S2 MSI measurements will provide a valuable and complementary data source of great interest, particularly to monitor coastal processes. Thought the repeat cycle of Sentinel-2A is quite long, - 10 days, the launch of Sentinel-2B in the next year will reduce it to 5 days. Furthermore, with interest growing in space-borne techniques for surface current and wave motion determinations, the proposed method can quantitatively provide very high-resolution information to help future developments.

Acknowledgements:

This work was supported through the ESA project SArONG under contract No. 4000117644/16/NL/FF/gp, and the Russian Science Foundation Grant No. 15-17-20020. The Copernicus Sentinel-2 data used in this paper are available at: https://scihub.copernicus.eu/dhus/#/home and http://www.ndbc.noaa.gov/ (for the buoy data).

References

Apel, J. R., H. M. Byrne, J. R. Proni, and R. L. Charnell (1975), Observation of oceanic internal and surface waves from the Earth Resources Technology Satellite, *J. Geophys. Res., 80, 865-881*

Barber, 1954, Finding the direction of sea waves, Nature, 174, 1048-1050

Bolshakov A.N., V.M. Burdyugov,, S.A.Grodsky, , V.N. Kudryavtsev (1988). The spectrum of energy containing surface waves as derived from sun glitter images. *Issledovaniya Zemli iz Kosmosa, 5*, 11-18 (in Russian)

Bolshakov, A. N., V.M. Burdyugov,, S.A.Grodsky, , V.N. Kudryavtsev, and V.G. Proschenko (1990a), Spectra of energy-carrying surface-waves using solar highlight images - comparison with in-situ data, *Earth Obs. Remote Sens*., **8**, 29-40.

Bolshakov, A.N. V.M. Burdjugov, .., S.A. Grodsky, and V.N. Kudryavtsev (1990b), 2-dimensional surface elevation spectra from airphoto data, *Izvestia, Atmos. Oceanic Phys.*, **26**, 652-658.

Bréon, F. M., and N. Henriot (2006), Spaceborne observations of ocean glint reflectance and modeling of wave slope distributions, *J. Geophys. Res. 111, C06005, doi:10.1029/2005JC003343.*

Chapron, B., V. Kerbaol, D. Vandemark, and T. Elfouhaily (2000), Importance of peakedness in sea surface slope measurements and applications, *J. Geophys. Res., 105, 17,195–17,202.*

Cox, C., and W. Munk (1954), Measurement of the roughness of the sea surface from photographs of the Sun's glitter. *J. Opt. Soc. Amer., 44*, 838–850.

Collard F., F. Ardhuin, and B. Chapron (2005), Extraction of Coastal Ocean Wave Fields From SAR Images. IEEE J. Ocean. engineering, 30, NO. 3.

Dugan, J. P., C. C. Piotrowski, *and* J. Z. Williams (2001), Water depth and surface current retrievals from airborne optical measurements of surface gravity wave dispersion, J. Geophys. Res., 106, C8, 16903–16915

European Space Agency (ESA), Sentinel-2: ESA's Optical High-Resolution Mission for GMES Operational Services, ESA SP-1322/2, March 2012, pp. 80, available from the European Space Agency, Noordwijk, the Netherlands, 2012.

Gelpi, C. G., B.C. Schuraytz,a nd M. E. Husman (2001). Ocean wave height spectra computed from high-altitude, optical, infrared images. *J. Geophys. Res.*, *106*, Cll, 31403-31413.

Genz, J., J. Aucan, M. Merrifield, B. Finney, K. Joel, and A. Kelen (2009), Wave navigation in the Marshall Islands: Comparing indigenous and Western scientific knowledge of the ocean, *Oceanography*, *22*, 2, 234–245, doi:10.5670/oceanog.2009.52

Hu, C., X. Li, W. G. Pichel, and F. E. Muller-Karger (2009), Detection of natural oil slicks in the NW Gulf of Mexico using MODIS imagery, *Geophys. Res. Lett., 36*, L01604, doi:10.1029/2008GL036119.

Jackson, C. (2007), Internal wave detection using the Moderate Resolution Imaging Spectroradiometer (MODIS), J. Geophys. Res., 112, C11012, doi:10.1029/2007JC004220.

Jackson, C. R., and W. Alpers (2010), The role of the critical angle in brightness reversals on sunglint images of the sea surface, J. Geophys. Res., 115, C09019, doi:10.1029/2009JC006037.

Kudryavtsev V., A. Myasoedov, B. Chapron, J. Johannessen, F. Collard (2012a). Joint sun-glitter and radar imagery of surface slicks, *Remote Sensing of Environment* doi:10.1016/j.rse.2011.06.029

Kudryavtsev V., A. Myasoedov, B. Chapron, J. Johannessen, and F. Collard (2012b), Imaging meso-scale upper ocean dynamics using SAR and optical data, *J. Geoph. Res.*, *117*, C04029, doi:10.1029/2011JC007492, 2012

Phillips, O.M. (1977), The Dynamics of the Upper Ocean, 2nd ed., *Cambridge Univ. Press*, New York

Rascle, N., B. Chapron, A. Ponte, F. Ardhuin, and P. Klein *(*2014*)*, Surface roughness imaging of currents shows divergence and strain in the wind direction*, J. Phys. Oceanogr.*, *44*, 2153–2163, doi*:*10.1175/JPO-D-13-0278.1

de Michele, M., S. Leprince, J. Thiébot, D. Raucoules, and R. Binet (2012), Direct measurement of ocean waves velocity field from a single SPOT-5 dataset. *Remote Sensing of Environment 119*, 266–271.

Stilwell, D. (1969), Directional energy spectra of the sea from photographs, *J. Geophys. Res.*, *74*, 1974–1986

Vandemark D., Vandemark, D., B. Chapron, J. Sun, G. H. Crescenti, and H. C. Graber (2004), Ocean Wave Slope Observations Using Radar Backscatter and Laser Altimeters, *J. Phys. Oceanogr.*, *34*, 2825-2842

Figures and Captions:

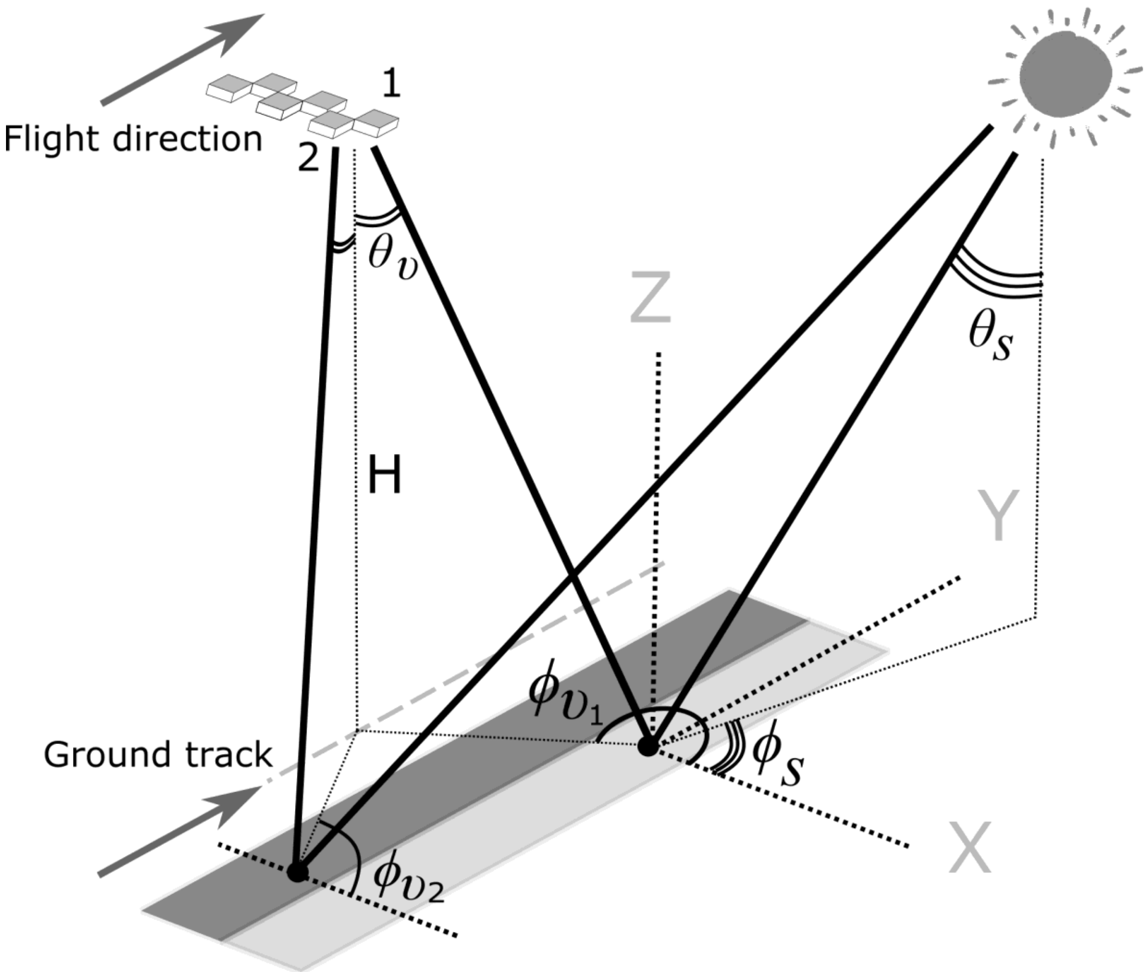

Figure 1. Sketch of S2 MSI viewing geometry

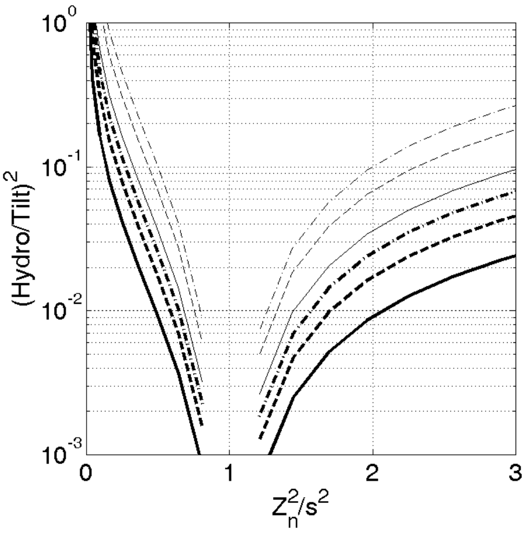

Figure 2. Ratio between hydrodynamic and tilt modulation contributions to the brightness spectrum defined by (11) as a function of Z_n^2/s^2, different wind speeds: (solid) 5 m/s, (dash) 10 m/s, and (dash-dotted) 15 m/s, and angles between wavenumber vector and direction of the brightness gradient: (thick lines) 0 deg., (thin lines) 60 deg.

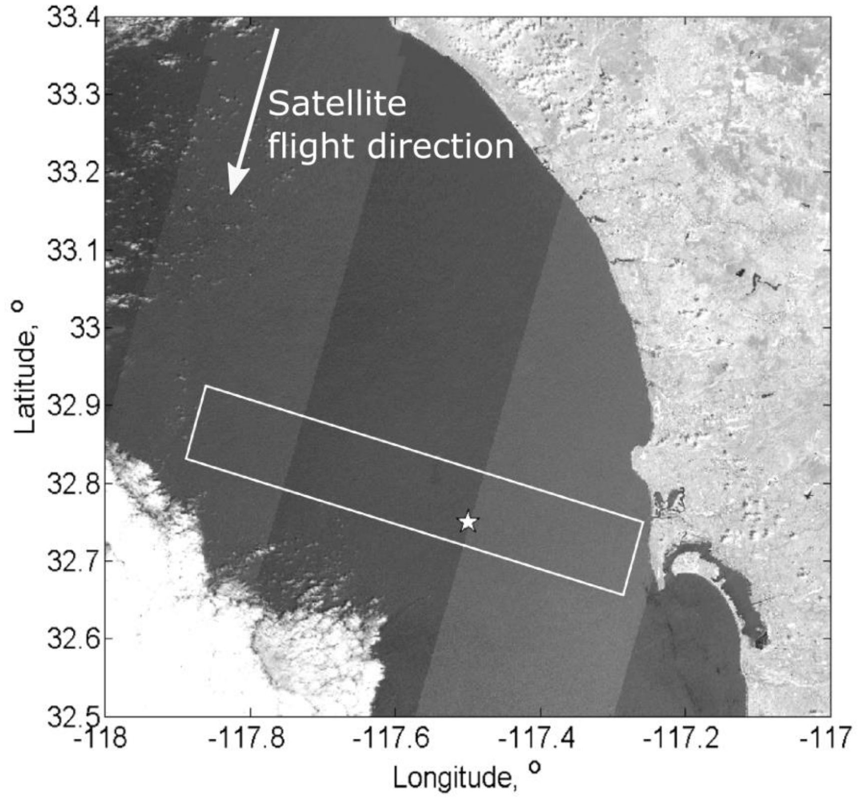

Figure 3. S2 MSI image channel B04 (665 nm) off the California coast, 2016-04-29 18:40. The large-scale striping in the image is due to the configuration of MSI detectors (see main text). The white star indicates location of the buoy 46258 - Mission Bay West CA (220), Scripps Institution of Oceanography. The white frame indicates the selected image fragment used for further analysis. Image contains modified Copernicus data (2016). Strips formed by odd and even detectors look brighter and darker, respectively.

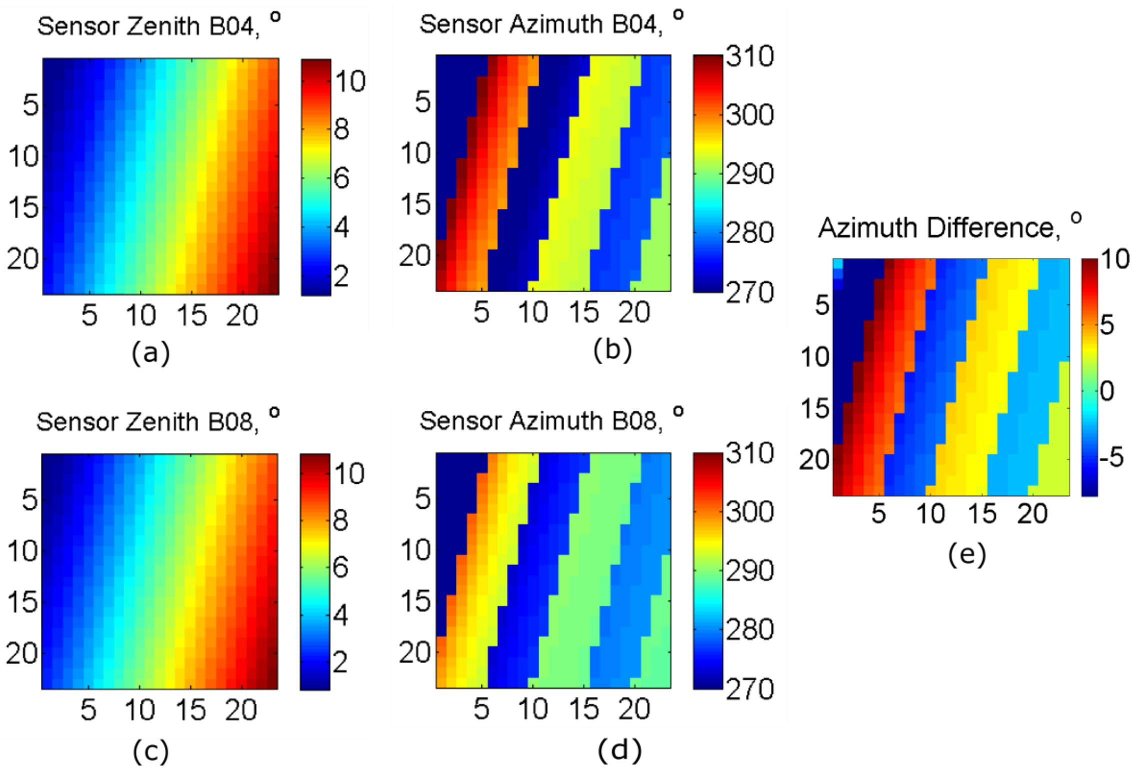

Figure 4. Sensor (a, c) zenith and (b, d) azimuth angles for the S2 scene shown Figure 3, for two channels, (upper row) B04, and (lower row) B08. (e) Azimuth difference between B04 and B08 shown in plots (b) and (d).

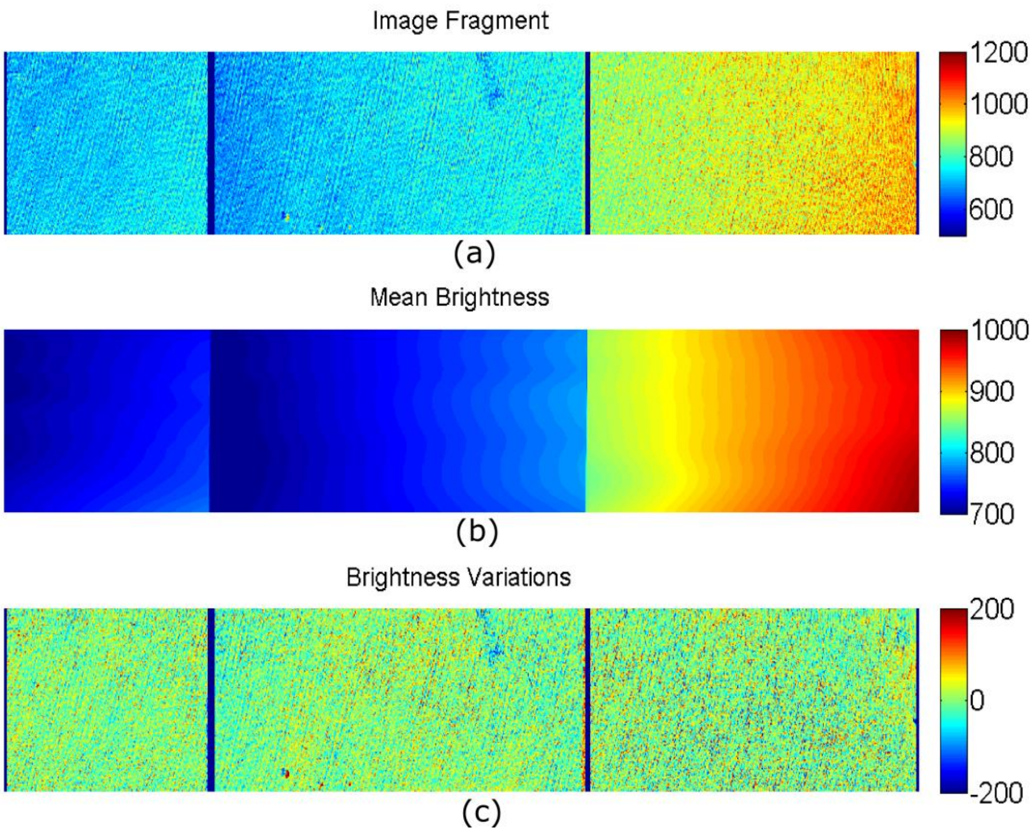

Figure 5. Sentinel-2 MSI SSGI brightness distributions for the white box shown in Fig. 3. (a) Surface brightness field inside the selected area, box shown Fig.3; (b) corresponding smoothed brightness field; (c) resulting brightness variation from the difference between original and smoothed fields.

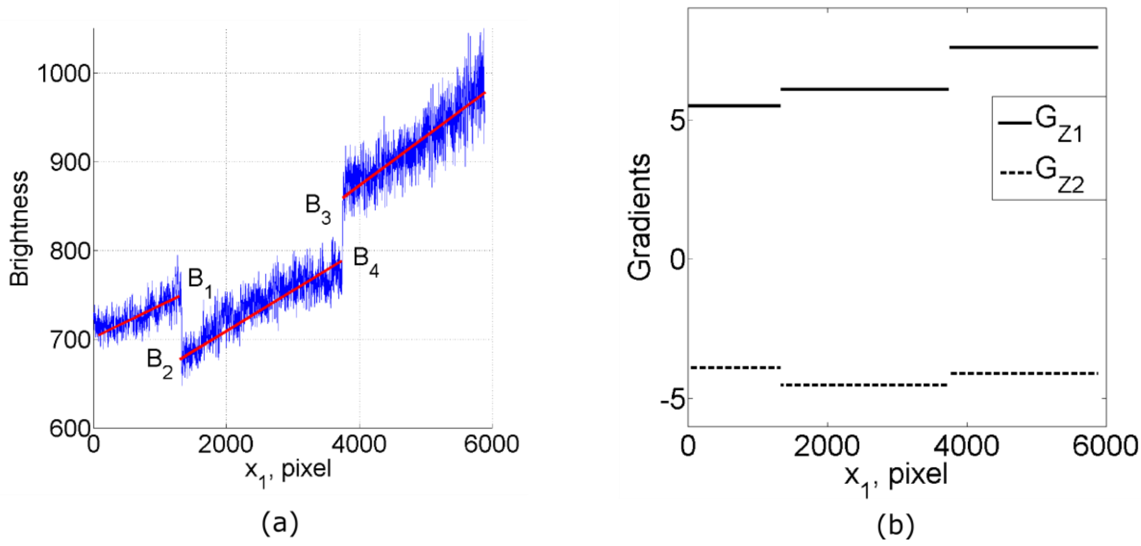

Figure 6. (a) Brightness field averaged over x_2-axis inside each stripe, with corresponding linear fits. (b) Components of the tilt transfer function G_{zx} and G_{zy} defined by (15) and calculated using the mean brightness gradients, shown in (a)

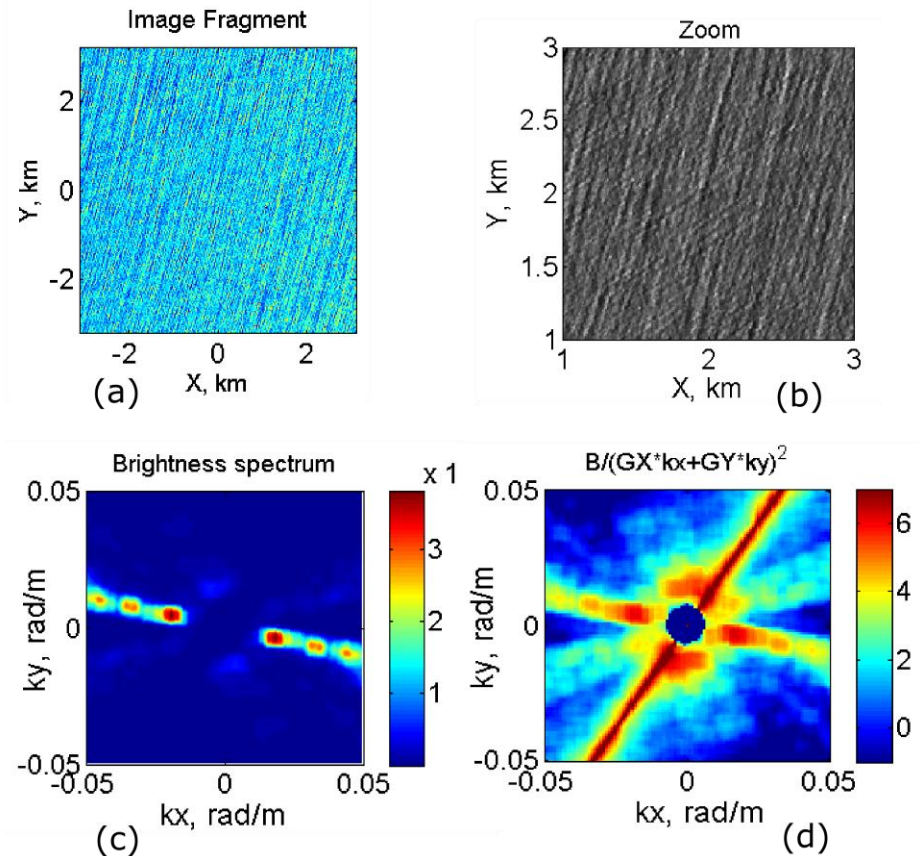

Figure 7. (a) S2 MSI image fragment from (Fig 5) and (b) its zoom, in which three wave systems can be detected; (c) SSGI brightness spectrum; (d) Wave elevation spectrum. The strong linear feature with abnormal "enhanced energy" in (d) corresponds to the singularity area, in the vicinity of $G_{zj}k_j = 0$, over which wave spectrum determination is impossible. Unlike the image fragments, the spectra are rotated, so that k_x-axis is directed to the east.

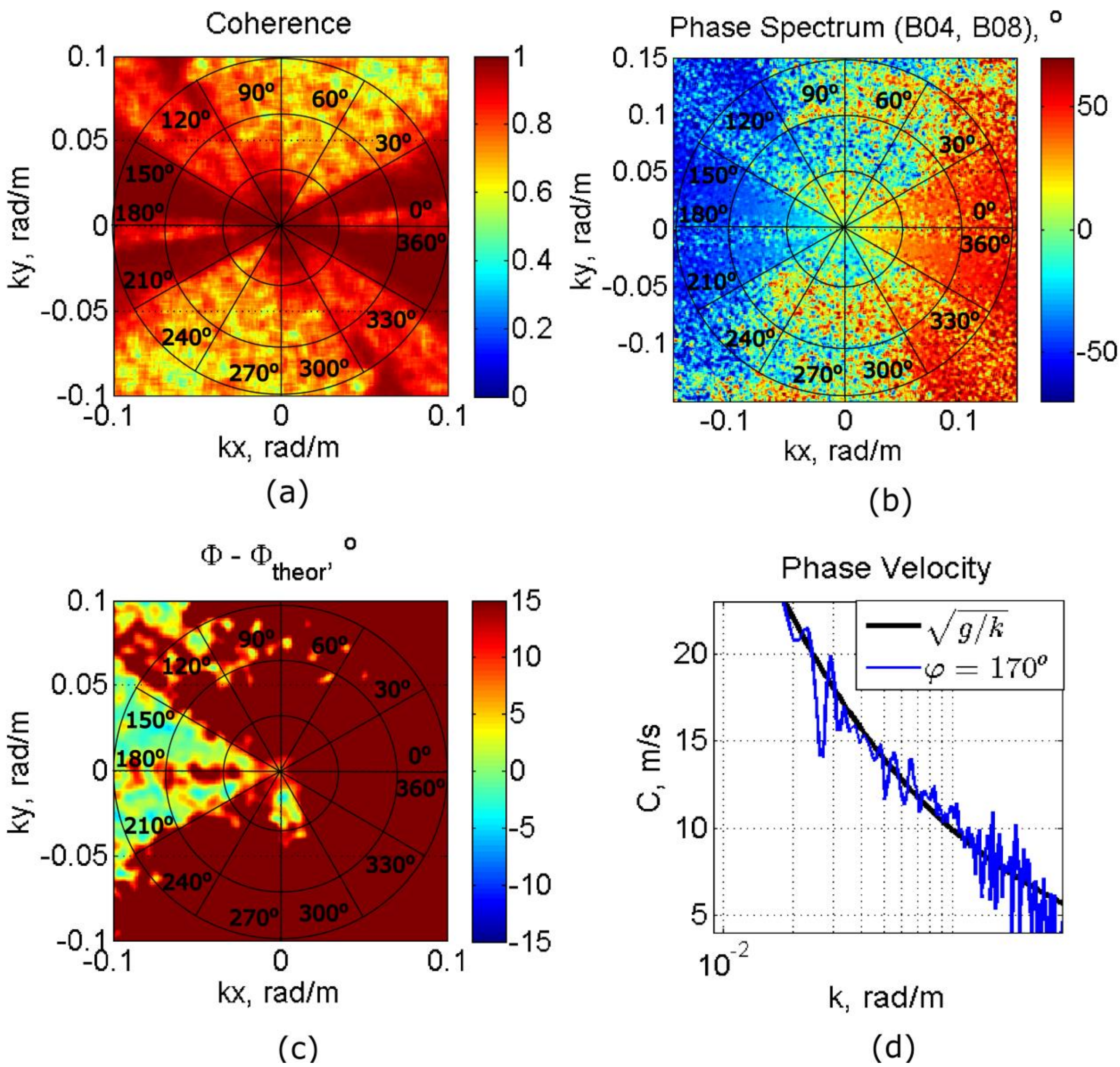

Figure 8. Spectrum of (a) coherence and (b) phase spectrum obtained from cross-spectral analysis between Sentiel-2 MSI channel B04 (664 nm) and B08 (864 nm). (c) Difference between measured phase shifts and predicted ones (21). The spectral domain where the difference is close to 0 indicates the "true" propagation direction of the wave components. (d) Dispersion relation, $c(k)$, derived from cross-channel analysis, eq.(22a), against the linear model relation $c = (g/k)^{1/2}$.

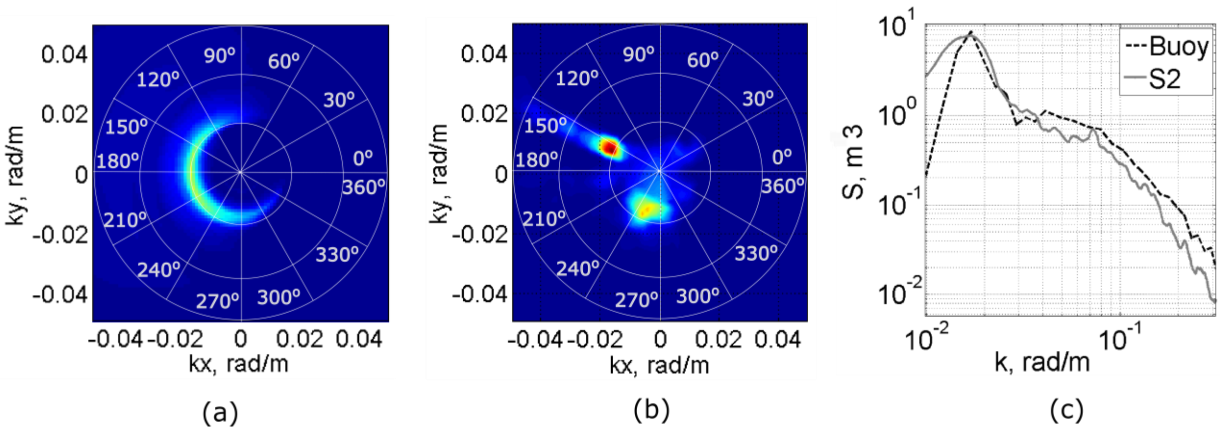

Figure 9. (a) Buoy directional spectrum, (b) spectrum derived from sun glitter image, and (c) omnidirectional spectra. kx-axis is directed to the East. Buoy and sun glitter derived SWH are 1.5 m and 1.4m, respectively. Buoy derived mean wave direction is 185°.

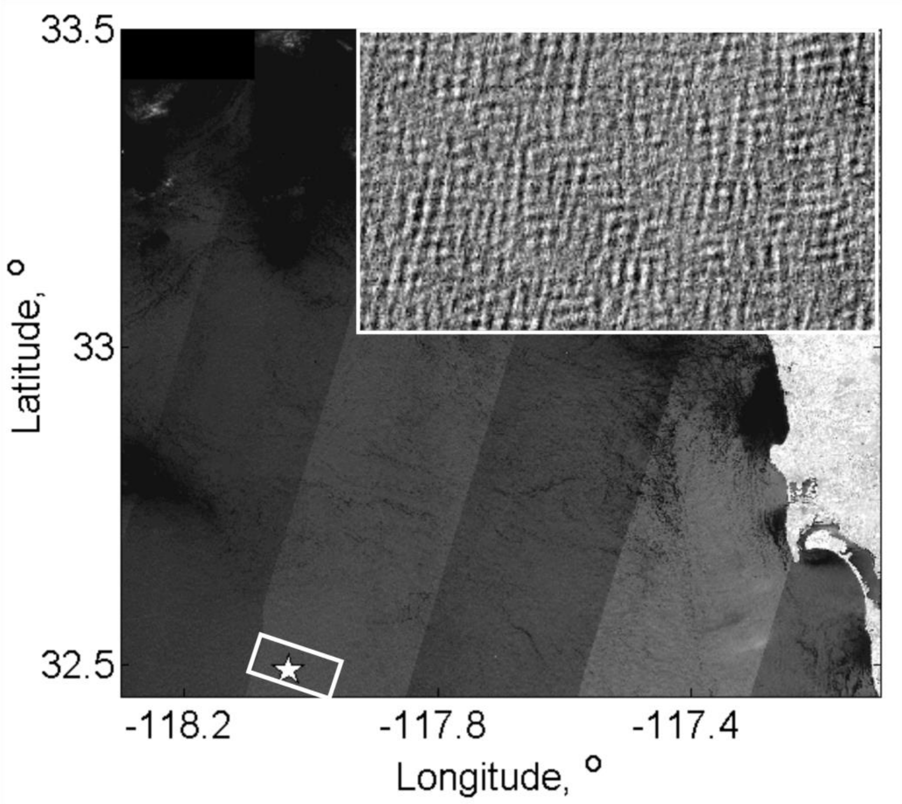

Figure 10. Sentinel-2 MSI image channel B04 off the California coast, 2016-04-19 18:44. The white star indicates location of the buoy 46086 - San Clemente Basin, National Data Buoy Center (NDBC). Wind speed is 3.3 m/s. The white frame indicates the selected image fragment, and insert is its zoom of that area. Contains modified Copernicus data (2016).

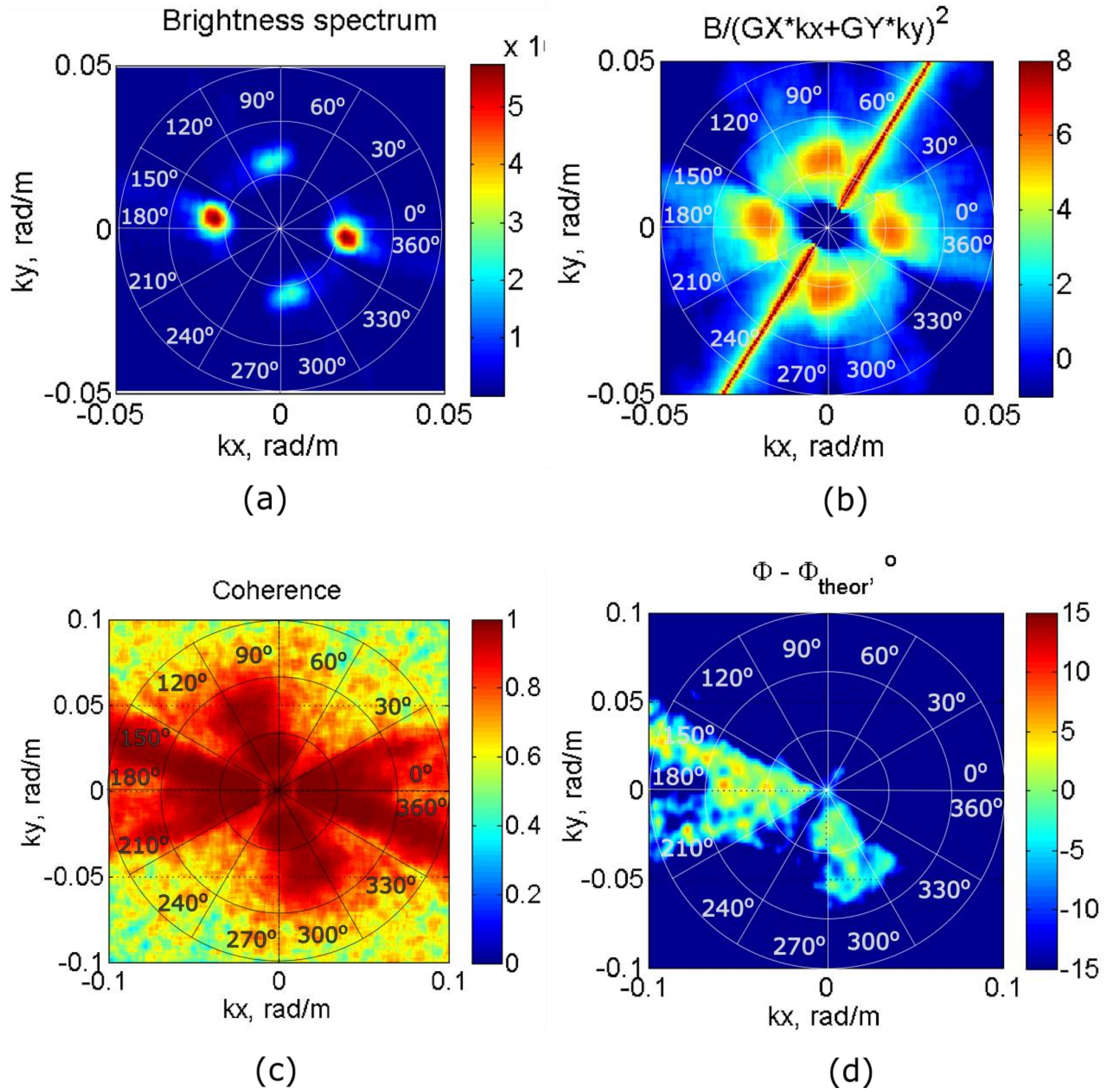

Figure 11. (a) Spectrum of the brightness modulations; (b) corresponding wave elevation spectrum; (c) Coherence spectrum between channels B04 and B08; (d) Difference between measured phase shifts and predicted by (21). Linear feature with abnormal "enhanced energy" in (b) corresponds to the singularity area, in the vicinity of $G_{zj}k_j = 0$, over which wave spectrum determination is impossible.

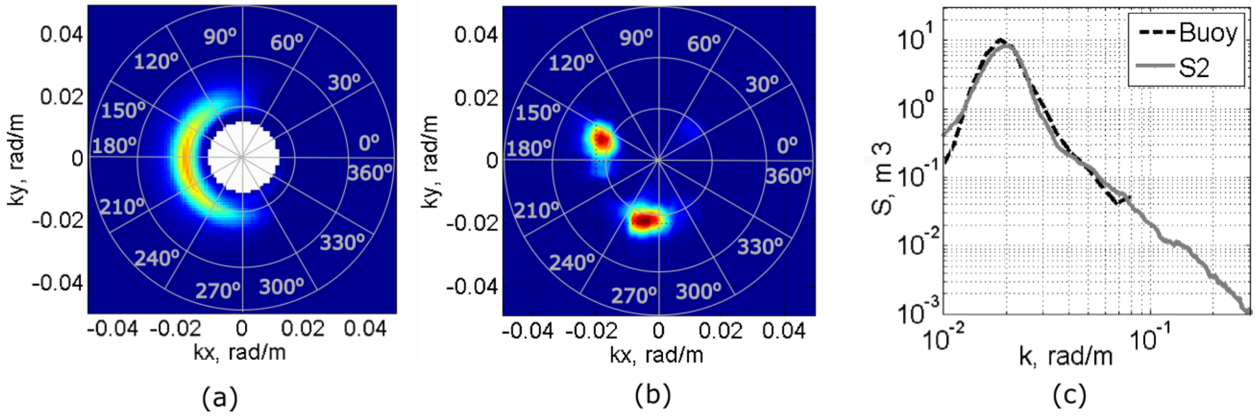

Figure 12. (a) Buoy directional spectrum, (b) spectrum derived from sun glitter image (b), and (c) omnidirectional spectra. kx-axis is directed to the East. Buoy and sun glitter derived SWH are 1.3 m and 1.2 m, respectively. Buoy derived mean wave direction is 185°.

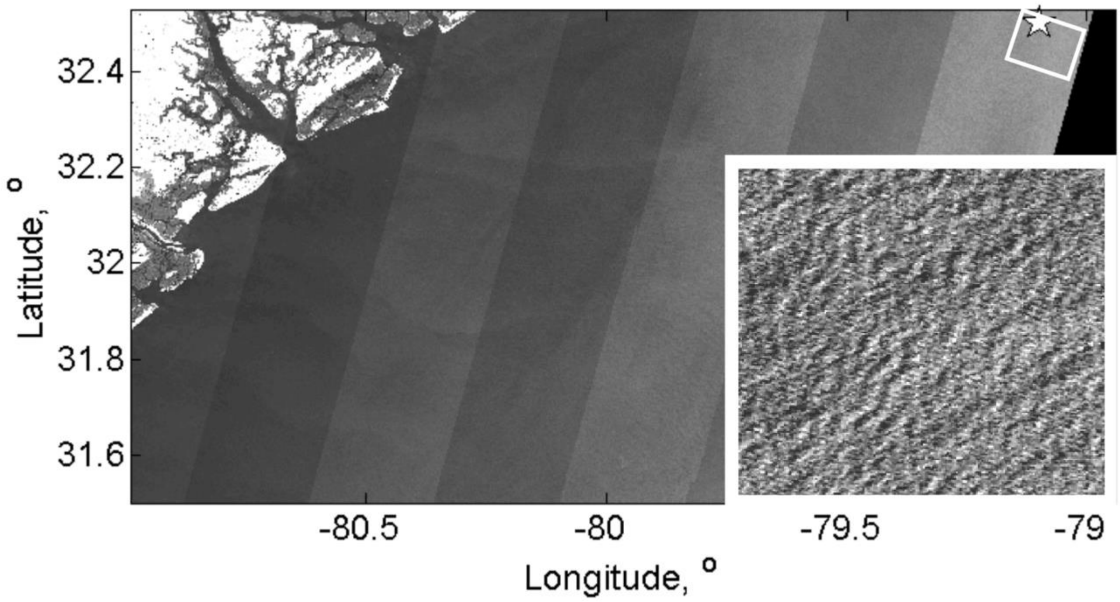

Figure 13. Sentinel-2 MSI image channel B04 off the Florida coast, 2016-05-14 16:04. Star indicates location of the buoy 41004 - Edisto, National Data Buoy Center (NDBC). Wind speed is 6.5 m/s. White frame indicates the selected image fragment, and insert is its zoom. Contains modified Copernicus data (2016).

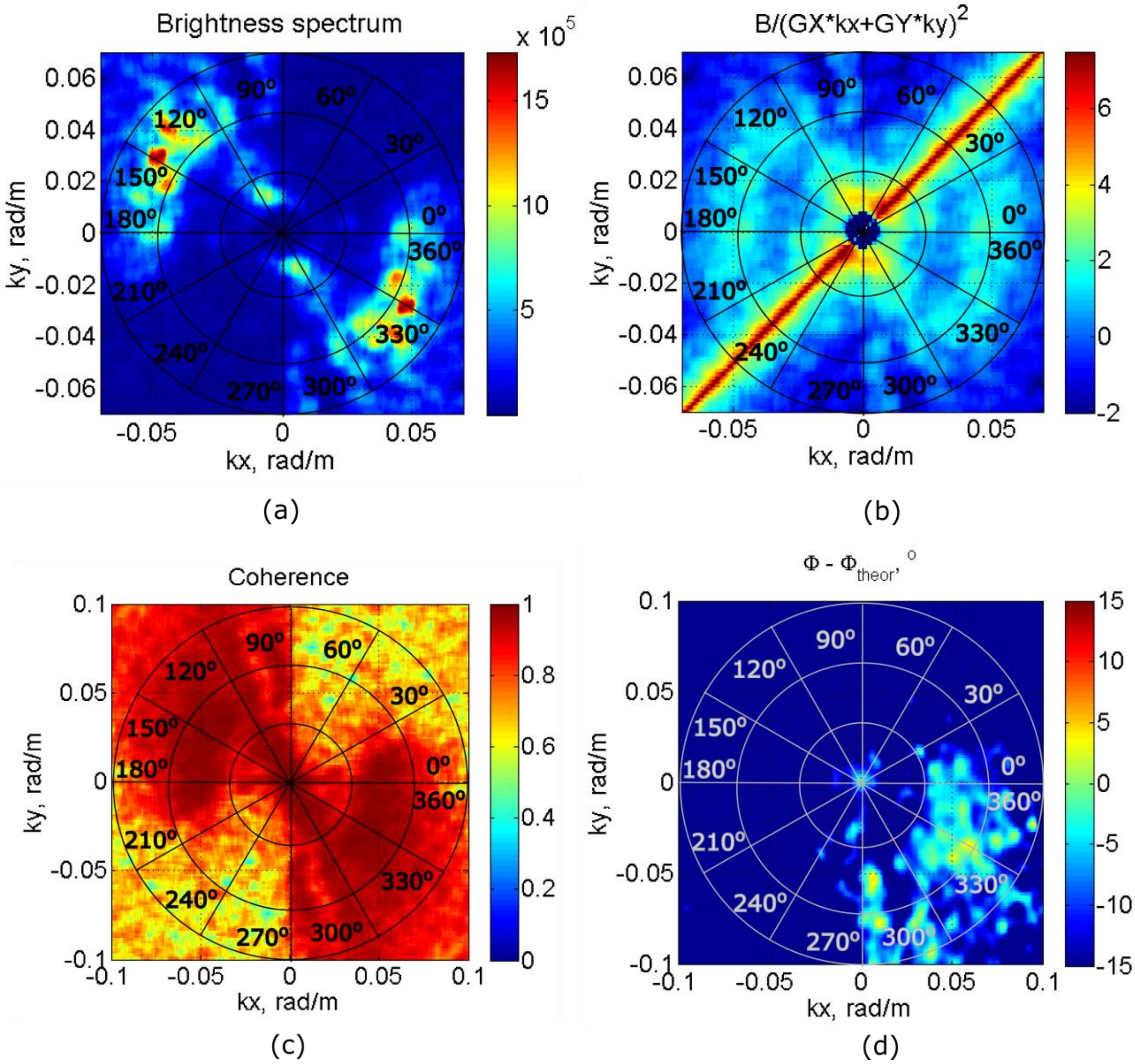

Figure 14. (a) Spectrum of the brightness modulations; (b) corresponding wave elevation spectrum; (c) Coherence spectrum between channels B04 and B08; (d) Difference between measured phase shifts and predicted by (21). Linear feature with abnormal "enhanced energy" in (b) corresponds to the singularity area, in the vicinity of $G_{zj}k_j = 0$, over which wave spectrum determination is impossible.

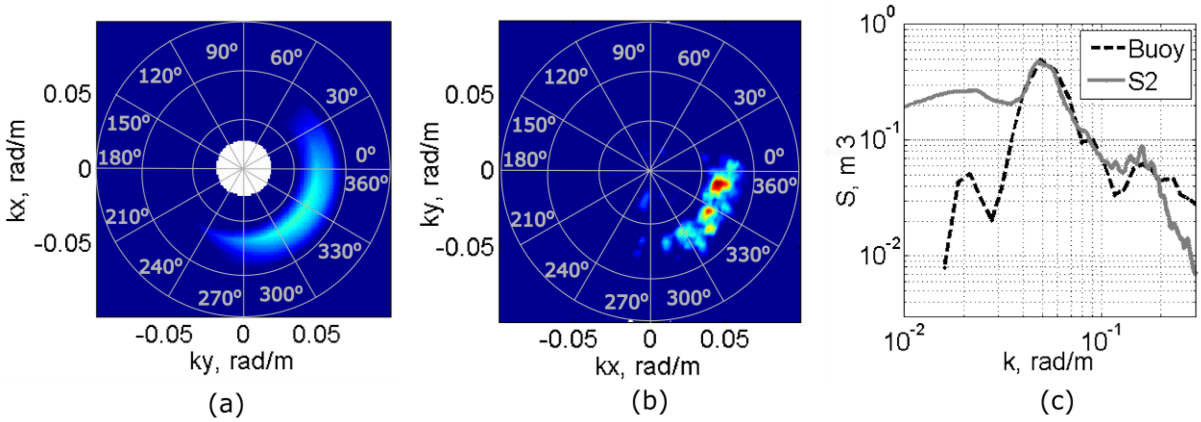

Figure 15. (a) Buoy directional spectrum, (b) spectrum derived from sun glitter image, and (c) omnidirectional spectra. kx-axis is directed to the East. Buoy and sun glitter derived SWH are 0.7 m and 0.6 m, respectively. Buoy derived mean wave direction is 322^{o}.